

Effect of heat treatments on fabricated Wire and arc additive manufacturing parts of Stainless steel 316: Microstructure and synchrotron X-ray Diffraction analysis

Authors: Tiago A. Rodrigues ^{a*}, Valdemar R. Duarte ^a, Jiajia Shen ^a, G. G. Ribamar ^b, Julian A. Avila ^b, Norbert Schell ^c, J. D. Escobar ^d, Telmo G. Santos ^a, J. P. Oliveira ^{a,1}

^a UNIDEMI, Department of Mechanical and Industrial Engineering, NOVA School of Science and Technology, Universidade NOVA de Lisboa, 2829-516 Caparica, Portugal

^b São Paulo State University (UNESP), Campus of São João da Boa Vista, Av. Prof.ª Isette Corrêa Fontão, 505, Jardim das Flores, 13876-750, São João da Boa Vista, SP, Brazil

^c Helmholtz-Zentrum Geesthacht, Institute of Materials Research, Max-Planck-Str. 1, Geesthacht, 21502, Germany

^d Metallurgical and Materials Engineering Department, University of São Paulo, Av. Prof. Mello Moraes 2463, 05508-030, São Paulo, SP, Brazil

*Corresponding author

Abstract

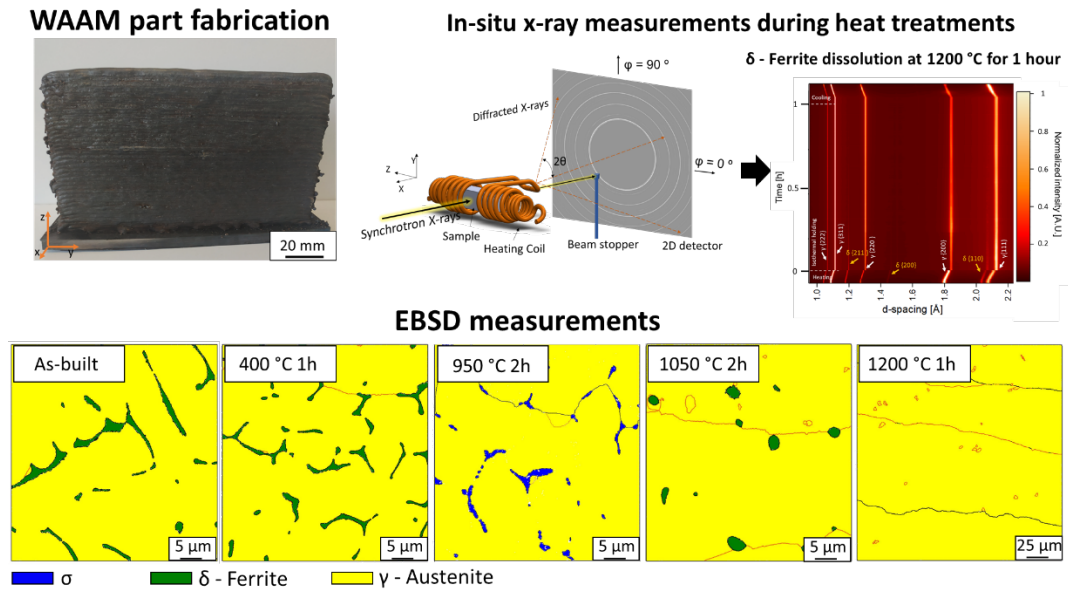
Different geometrical features and intricate parts can now be fabricated by wire and arc additive manufacturing (WAAM). Even though a broad range of applications rises with this technology, the processed metallic materials still follow metallurgy rules. Therefore, undesired phases may appear during the multiple thermal cycles affecting the fabricated part. One of the most used stainless steel in the industry is the 316L, which provides a combination of high corrosion resistance and mechanical properties. In this study, 316L stainless steel walls were fabricated by WAAM and submitted to several heat treatments to understand the precipitation kinetics of secondary phases and observe the δ -ferrite dissolution with synchrotron X-ray diffraction measurements. The as-built samples presented δ – ferrite dendrites in an austenite matrix. In-situ observations showed σ precipitation during the first minutes of isothermal holding at 950 °C, from direct precipitation on the δ -ferrite islands. Solubilization heat treatments at 1050 and 1200 °C resulted in an undissolved amount of ferrite of approximately 6.5 % and 0.4 %, respectively.

¹ **Statement on Conflicts of Interest:** One of the authors of this article is part of the Editorial Board of the journal. To avoid potential conflicts of interest, the responsibility for the editorial and peer-review process of this article lies with the journal's other editors. Furthermore, the authors of this article were removed from the peer review process and had no, and will not have any access to confidential information related to the editorial process of this article.

respectively. The amount of δ – ferrite showed a direct relationship with the hardness values. This work combined advanced materials characterization and thermodynamic calculations to rationalize the microstructure evolution upon the use of heat treatments in WAAM-fabricated 316L stainless steel parts.

Keywords: wire and arc additive manufacturing; stainless steel; sigma phase; in-situ phase transformation, high energy synchrotron x-ray diffraction

Graphical Abstract



Highlights

- Different heat treatments were performed on stainless steel 316 WAAMed parts
- σ -phase precipitation is observed in-situ via high energy synchrotron X-ray diffraction
- σ -phase starts to precipitates during the first minutes of isothermal holding at 950 °C in the δ -ferrite grains
- The amount of δ -ferrite decreased with an increase in the solubilization temperature.
- Eddy current testing is capable to differentiate δ – ferrite and σ phases.

1.Introduction

Austenitic stainless steels (ASS) are widely used in several industrial applications, including nuclear energy [1]. For example, parts of the reactor core in nuclear applications are exposed to high strength and corrosion environments at operating temperatures between 280-550°C [1]. The mechanical strength of ASS is reduced considerably above 500°C [2], and the fatigue crack propagation accelerates under operational temperatures above 150°C [3].

Precisa de uma conexão entre o parágrafo anterior e a manufatura aditiva.

Regarding additive manufactured samples of ASS, Lou et al. [3] highlight the necessity of producing an equiaxed microstructure through high-temperature recrystallization annealing, which increases the corrosion fatigue resistance in environments consisting of high-temperature water exposure (288°C).

Notice that new fabrication processes have different types of microstructures, and therefore various corrosion and mechanical responses. Wire and arc additive manufacturing (WAAM) is not the exception. Still, little information is available. Essa frase está muito aberta, não acho que esteja entregando muito valor e não sei se tenha referências.

WAAM is a variant within the additive manufacturing techniques, based on the fundamentals of welding [4], where a wire feedstock material is melted by an electric arc and deposited in a layer-by-layer fashion. WAAM features high deposition rates and high material efficiency (o que significa material efficiency), which is interesting for building large components for industrial applications, such as for the oil and gas, and nuclear sectors. However, poor dimensional accuracy and different microstructures are obtained compared to laser powder bed fusion AM, a more widespread AM variant (qual é a necessidade dessa última frase criticando o WAAM? Acho que não precisa).

Austenitic stainless steels manufactured by WAAM typically exhibit delta-ferrite (δ) within the austenitic (γ) matrix [ref]. The multiple heating/cooling cycles during WAAM, combined with the long soaking times at high temperatures, affect the microstructure evolution in WAAM fabricated parts [9].

Some authors found that δ -ferrite can prevent hot cracking by accommodating large amounts of pure S and P in the interdendritic areas [5–8].

Esse paragrafo precisa começar definindo coisas que são conhecidas:

It is well known that improper thermomechanical processing of austenitic stainless steels can lead to undesired secondary precipitation. During welding, a common undesired consequence of multi-deposition sequences between 590-900°C is the formation of Cr-rich carbides (...) [refs], as well as the potential secondary precipitation of intermetallic deleterious phases, such as sigma [ref], chi [ref], Laves [ref]. Especially regarding arc welding, it has been largely reported that the as welded microstructures in austenitic stainless steel may contain precipitates, such as ... [refs]. The presence of delta ferrite is also reported after arc welding of austenitic stainless steels due to... [refs].

For (austenitic?, ferritic? Martensitic? All?) stainless steels, soaking times between 550-900 °C promote the formation of Cr-rich carbides ($M_{23}C_6$ and M_7C_3). Additionally, other deleterious intermetallic phases encountered after WAAM? AM? Welding? include the sigma phase (σ) [10,11], chi phase (χ) [12–14], and Laves phase [15]. The σ phase leads to hardening and embrittlement in stainless steels and therefore have received particular attention [16,17]. This phase can precipitate within 500 and 950 °C during welding, rolling, and forging cycles [15]. In addition, the σ phase consumes chromium and molybdenum from the γ matrix, deteriorating its corrosion resistance [18].

During WAAM, microstructures similar to those obtained after conventional arc welding can be expected. Additive manufacturing through LPBF, WAAM... etc, of austenitic stainless steels have shown microstructures composed of... [refs]. These non-equilibrium microstructures impair corrosion resistance and result in hardening and embrittlement of austenitic stainless steels [refs]. It has been also discussed that delta ferrite can serve as nucleation sites for further precipitation of $M_{23}C_6$ and sigma upon annealing cycles around 720 °C [refs]. However, proper annealing cycles around xx °C can provide complete dissolution of delta ferrite, avoiding the formation of secondary precipitates. The presence of compositional segregations and delta ferrite are mostly unavoidable and therefore understanding the microstructural evolution of as built ASS after WAAM is currently a topic of great interest for the additive manufacturing community. Synchrotron X-ray diffraction measurements are specially useful in this case to understand the kinetics of phase transformations during the execution of annealing cycles.

Hence, heat treatments are needed to improve the corrosion and mechanical properties of AM ASS [3], and the understanding of phases evolution of ASS during heat treatments application will contribute to choosing better microstructural features.

This study investigates the phase transformations in a xx austenitic stainless steels after WAAM using synchrotron x ray diffraction. The kinetics of δ -ferrite dissolution was studied during post-WAAM annealing cycles at 400, 950, 1050 and 1200 °C. Complementary EBSD analysis was performed to confirm the morphology, size and distribution of delta ferrite and sigma phases before and after annealing. Microhardness and Eddy current... measurements were used to Our observations provide new understanding on the effects of time and temperature on the microstructural evolution of as-built ASS, and can be useful to design or optimize heat treatment routes relevant to additively manufactured parts.

2. Materials and methods

2.1 Experimental setup

In this study, WAAM single-walls were fabricated using an in-house custom-made WAAM apparatus, which included a customized gas metal arc welding (GMAW) torch. The wire feedstock used in this work was a commercial 316L stainless steel wire (ER 316LSi) with a diameter of 1 mm. The chemical composition of the feedstock wire is detailed in Table 1. A WAAM wall with 180 x 110 x 8 mm was built with a wire feed speed of 4 m/min and a travel speed of 300 mm/min. A voltage of 19.5 V was used, and the molten pool was protected with 99.99 % Argon. A zig-zag deposition strategy with 90 seconds of idle time between each torch stop/start was selected to build the 75-layer WAAM part.

Table 1 - Chemical composition of the ER 316LSi wire electrode (wt.%).

| C | Mn | Si | Ni | Cr | Mo | Cu | Fe |
|----------|-----------|-----------|-----------|-----------|-----------|-----------|-----------|
| 0.03 | 1.60 | 0.65 | 11 | 18.5 | 2.50 | 0.75 | Bal. |

2.2 In-situ synchrotron x-ray diffraction during heat treatments

Four post-WAAM heat treatments (PWHT) were performed in-situ at the High Energy Materials Science beamline at PETRA III, DESY (Hamburg, Germany) with a beam energy of 100 keV (0.1234 Å). Material expansion/shrinkage during heating and cooling was measured using a modified Bähr DIL-805 dilatometer filled with Argon to avoid oxidation during the heat treatments.

The four different heat treatments were performed as follows: HTT#1 consisted of a stress relief heat treatment at 400 °C for 1 hour, followed by air cooling; HTT#2 aimed at promoting σ phase precipitation and was performed at 950 °C for 2 hours, followed by forced gas (Ar) cooling; HTT#3 was performed at 1050 °C for 2 hours, followed by forced gas (Ar) cooling; while HTT#4 was performed at 1200 °C for 1 hour, also followed by forced gas (Ar) cooling. It should be noticed that the selection of imposing forced gas cooling aimed at avoiding the precipitation of intermetallics after the termination of the high-temperature plateau. All conditions were heated up to the target treatment temperature at a rate of 20 °C/s. As for the cooling conditions, HTT#1 had a cooling rate of 5 °C/s, while for the remaining heat treatments, a cooling rate of 20 °C/s was imposed.

A schematic representation of the heat treatments performed and the in-situ setup used are depicted in Figure 1 and Figure 2. The primary purpose of the synchrotron experiments was to determine the δ -ferrite dissolution and the kinetics of secondary phase formation/dissolution during the selected heat treatments.

A 2D Perkin Elmer detector was used to capture the Debye-Scherrer diffraction rings. These were then integrated along the full azimuthal angle (φ) using freely available Fit2D software [19] to obtain conventional (Intensity vs. d-spacing) diffraction patterns. The beam size was 1 x 1 mm, and the raw diffraction rings were captured every 10 seconds.

An in-house python-based routine was used to fit the diffraction peaks. The python routine used a Python package named *xrdfit* [20], which implemented a *Pseudo-Voigt profile function to fit peaks* and extract the analyzed data in this study, i.e., the peak position, full width half maximum, and area under the fitted peaks. This information was then used to quantify the current phases at any given point during the heat treatments, following Faria et al. [21] methodology.

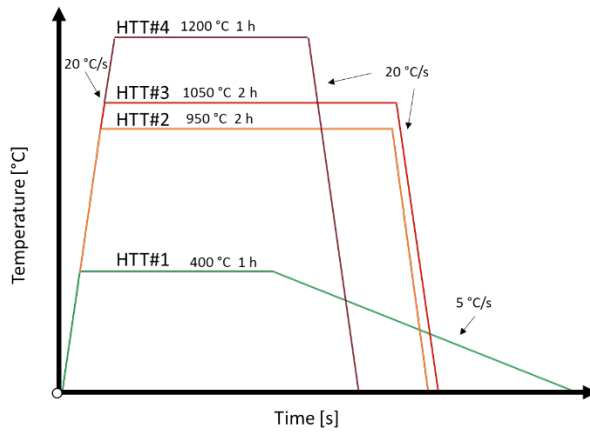


Figure 1 - Schematic representation of the heat treatments applied during In-situ Synchrotron X-ray diffraction measurements. The time-temperature plot also resumes the heating and cooling ramps used.

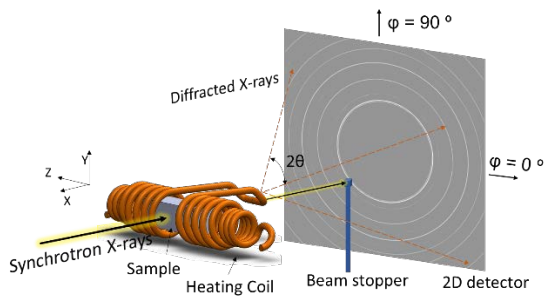


Figure 2 - Schematic representation of the experimental setup applied to perform the in-situ heat treatments.

2.3 Microstructural characterization

All conditions, including the as-built WAAM walls, were analyzed via optical and scanning electron microscopy, hardness testing, and electrical conductivity measurements. For the microscopy observations, samples were polished using abrasive papers with grit from 80 to 2000 and polished using a 3 μm diamond suspension. Vilella's reagent was used to reveal the microstructure. A Leica DMI 5000 M optical microscope and an FEI Quanta FEG – Inspect-F50 scanning electron microscope equipped with an electron backscatter diffraction (EBSD) camera were used in this investigation. A python-based routine was used to calculate the percentage of each phase based on at least three optical microscopy images on the microstructure images. From this routine, the average and associated standard deviations were determined. EBSD measurements were carried out using an acceleration voltage of 20 kV and a step size of 150 nm.

Hardness measurements were performed using a Mitutoyo HM-112 Hardness Testing Machine, under a load of 0.5 N for 10 s across the sample's total height, with a distance between indentations of 500 μm . Magnetic permeability measurements were performed using an absolute helicoidally shielded eddy current (EC) probe with a 3 mm diameter, operating in bridge mode. The measurements were calibrated so that only the imaginary part of the electrical impedance of the probe conferred changes in the magnetic permeability of each sample. To measure the changes in electrical conductivity between samples, a four-point potential drop technique was used. Measurements were made across the full height, starting in the substrate. The probe has a needle spacing of 635 μm , and a current of 80 mA was imposed between the external needles. Hardness and EC measurements were used as an indirect sense of the microstructural changes in the samples' height and between conditions.

Figure 3 details the position within a given WAAM wall where specimens were taken for microstructure and mechanical characterization.

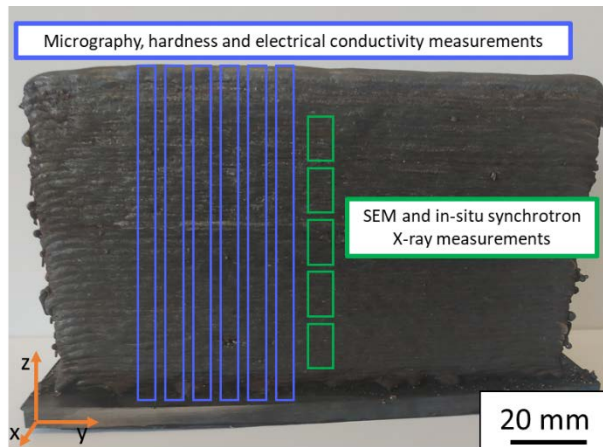


Figure 3 - Localization of the specimens taken from the Stainless steel 316 part, for microstructure and mechanical characterization.

3. Results and discussion

3.1 Macroscopic characterization

Figure 4 a) shows a micrograph of the as-built sample with primary dendrites composed of δ -ferrite aligned with the solidification direction (z-axis). Micrographs of the produced samples are depicted in Figure 4 b) to f). The as-built condition (Figure 4 b) is characterized by δ -ferrite dendrites oriented perpendicular to the deposition direction in an austenitic (γ) matrix. After

the stress relief heat-treatment, the microstructure maintained similar characteristics to that of the as-built condition (Figure 4 c). With the increase in the heat treatment temperature to 1050 °C, the columnar features became more unnoticeable, with the dissolution of dendrites arms (Figure 4 e). Finally, when the heat treatment was set to 1200 °C, almost no evidence of the original solidification microstructure of the as-built material exists. Only some tiny islands of residual ferrite dispersed in the matrix are depicted (refer to Figure 4 f).

Figure 4 a) depicts a variation in the morphology of ferrite as the number of layers increases. Typically, layers comprise skeletal-type ferrite in the non-remelted area and lathy-ferrite in the remelted area between layers [22,23], which is explained by the higher cooling rates in the remelted zone, since it is the first portion of volume to solidify [24].

Stainless steels solidify in one of four possible ways: mode A - single-phase austenite (Liquid \rightarrow Liquid + $\gamma \rightarrow \gamma$); mode AF - austenite with secondary ferrite (Liquid \rightarrow Liquid + $\gamma \rightarrow$ Liquid + γ + $\delta \rightarrow \gamma$ + δ); mode FA - primary ferrite with secondary austenite (Liquid \rightarrow Liquid + $\delta \rightarrow$ Liquid + δ + $\gamma \rightarrow \delta$ + γ); and mode F - single-phase Ferrite (Liquid \rightarrow Liquid + $\delta \rightarrow \delta$) [24]. The determination of the solidification mode can be based on the chromium to equivalent nickel ratio Cr_{eq}/Ni_{eq} . For the material used in this work, the Cr_{eq}/Ni_{eq} ratio is 1.69 and, considering Schaeffler's diagram. The solidification microstructure should be composed of austenite with a ferrite content ranging from 5 to 10 %. Under equilibrium solidification conditions, the austenitic stainless steel should present a ferritic-austenitic (FA) solidification mode, in which δ ferrite is the leading phase, and austenite being the second phase that begins to form between the liquid and δ -ferrite dendrites in a peritectic reaction [25]. Austenite will continue to solidify from the rest of the melt afterward. The diffusion-controlled δ to γ transformation will continue during cooling and stop when the diffusion is no longer possible, resulting in a skeletal and lathy ferrite type [26].

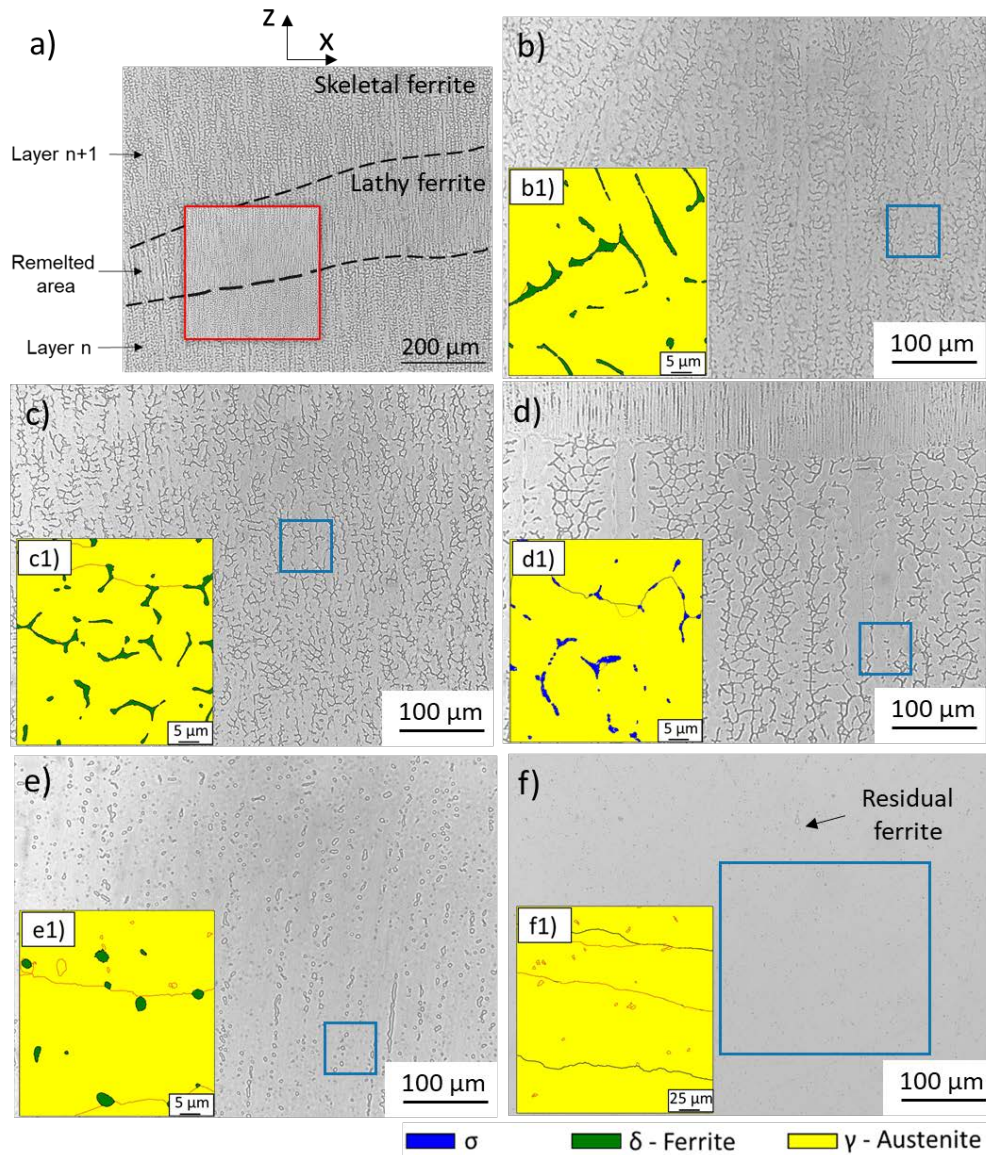


Figure 4 – a) and b) As-built, c) 400 °C 1h, d) 950 °C 2h, e) 1050 °C 2h f) 1200 °C 1h. Inserts b1, c1, d1, e1 and f1 correspond to the high magnification EBSD analysis.

3.2 Electron backscatter diffraction analysis

Figure 4 inserts depict the electron backscatter diffraction (EBSD) phase maps for each condition. As-built and stress relieved (400 °C / 1h) samples contain vermicular-type ferrite dispersed in the austenite matrix. The sample heat-treated at 950°C exhibits σ -phase both in a vermicular-type structure and along the grain boundaries. The increase in the temperature to 1050 °C revealed a lower fraction and size of delta-ferrite, as only small islands are present. In the 1200 °C condition, δ completely disappeared from the WAAMed stainless steel part.

Sigma phase can take up to thousands of hours to precipitate directly from γ austenite [24]. Padilha et al. [28] found in a creep test performed at 600 °C, that σ precipitation in austenite only occurred after 5481 h. The following reasons explain the low kinetics of σ precipitation from austenite: i) low solubility of C and N within the σ phase, which causes carbides and nitrides to form instead of promoting the σ phase transformation; ii) very slow diffusion of substitutional elements in the γ phase; and iii) different crystal structures between σ and austenite, which hinders nucleation of the former. This lack of lattice coherence, as well as the high interfacial energy between both phases, is the reason that leads to increased interface cracking when σ is present in these materials [17]. Contrarily, the σ phase was found to precipitate very quickly from residual δ -ferrite [13]. It prefers high Cr-concentrated regions, present in higher quantities in δ -ferrite can diffuse easily in its BCC structure [29].

Perron et al. [11] proposed three mechanisms for the precipitation of σ -phase: i) it involves nucleation at the γ/δ interface, which is a high interface energy site place beneficial for heterogeneous nucleation, and also a high Cr-region; ii) direct precipitation in the corners or triple points in the δ - ferrite, resulting from the Cr, Mo, and Ni concentration profiles; iii) eutectoid decomposition of δ -ferrite onto the σ phase and γ austenite ($\delta \rightarrow \sigma + \gamma$). Other nomenclatures exist; however, this partitioning is very similar to the one already described in the literature [17,30].

Due to the preservation of the ferrite vermicular-type showed in the micrographs and the EBSD maps (refer to Figure 4 d) it can be perceived that the appearance of σ -phase results from direct precipitation on the δ -ferrite islands. By precipitating within the δ -ferrite, the σ phase consumes the Cr content and ultimately occupies the entire δ -ferrite islands.

The percentage of δ -ferrite and σ phase content was calculated from the optical microscope images previously depicted in Figure 4 with a Python routine, and the results are presented in Table 2. The percentage of δ -ferrite in the as-built sample, heat-treated at 400 °C, and heat-treated at 1050 °C sample, is respectively 16.9, 17, and 2.8 %. The percentage of sigma in the sample heat-treated at 950 °C is around 16.8 %. Regarding the undissolved δ -ferrite in the sample heat-treated at 1200 °C, the δ -ferrite is below 0.5 %.

Table 2 – Phase percentage measurements made with a Python routine of each phase based on three different micrographs of each condition.

| Condition | γ | δ - Ferrite | σ |
|-----------|----------|--------------------|----------|
| As-built | 83.1 | 16.9 | - |

| | | | |
|-------------------|------|-----|------|
| 400 °C 1h | 83 | 17 | - |
| 950 °C 2h | 83.2 | - | 16.8 |
| 1050 °C 2h | 97.2 | 2.8 | - |
| 1200 °C 1h | 99.5 | 0.5 | - |

3.3 Synchrotron X-ray diffraction analysis

3.3.1 Ex-situ microstructural characterization

Figure 5 depicts the diffraction patterns of the as-built sample and those after completion of the selected heat treatments. In the as-built sample, diffraction peaks corresponding to the austenite and ferrite phases are identified. Even though WAAM parts are kept at high temperatures for long periods during fabrication, no carbides or other undesirable phases than δ - ferrite were detected in the as-built sample.

Precipitation of σ -phase was confirmed after two hours at 950 °C. Multiple diffraction peaks corresponding to the σ phase are evidenced in the orange spectra of Figure 5. An apparent reduction in the intensity of the δ -ferrite peaks is observed after heat treatment at 1050 and 1200 °C. The insert in Figure 5 illustrates that δ -ferrite is still present after being heat-treated at 1050 °C.

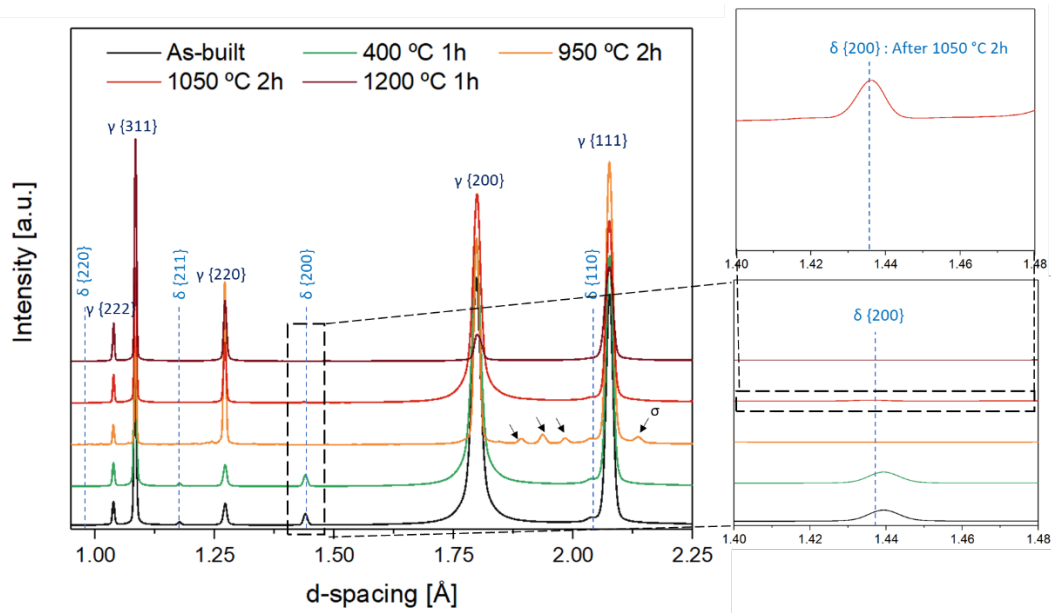


Figure 5 - Overview of the diffraction patterns of the as-built and heat-treated samples. Inserts illustrate the existence of delta-ferrite after heat-treated for two hours at 1050 °C.

Table 3 shows the evolution of the d-spacing for several diffraction peaks of both austenite and ferrite phases after the stress-relief heat treatment. It is interesting to note the shift of both ferrite and austenite peaks to higher d-spacing values (or correspondingly to lower scattering angles), indicating a change in the microstrain state, as typically for post-processing heat treatments [31].

Table 3 - D-spacing values of the main austenite and δ -ferrite peaks before and after stress-relief heat treatment (400 °C for 1 h).

| Peak | d-spacing [Å] | | Δ d-spacing [Å] |
|----------------|---------------|---------------|------------------------|
| | As-built | Stress-relief | |
| γ {311} | 1.0835 | 1.0845 | 0.001 |
| δ {211} | 1.1742 | 1.1758 | 0.0016 |
| γ {220} | 1.2709 | 1.2714 | 0.0005 |
| δ {200} | 1.4362 | 1.4397 | 0.0035 |
| γ {200} | 1.7967 | 1.7983 | 0.0016 |
| δ {110} | 2.0413 | 2.0435 | 0.0022 |
| γ {111} | 2.0742 | 2.0810 | 0.0068 |

3.3.2 In-situ phase transformations

- Precipitation of σ from δ -ferrite at 950 °C

Figure 6 a) details the evolution of several diffracted σ planes ($\{202\}_\sigma$, $\{420\}_\sigma$, $\{411\}_\sigma$, and $\{311\}_\sigma$) during the first hour of isothermal holding at 950 °C. In this experiment, it was observed that the σ phase started to precipitate during the first minute at isothermal holding. Qualitatively it was observed in Figure 6 a) that after 15 minutes of heat treatment at 950 °C, the $\{110\}_\delta$ peak disappeared and the $\{202\}_\sigma$ overlapped, appearing in the previous location occupied by the $\{110\}_\delta$ peak. However, due to the peak broadening of the σ reflection, which decreases over time, and due to the existence of $\{200\}_\delta$ peak after 60 minutes (refer to Figure 6 b), it is evidenced that the partial transformation of ferrite to σ does not cease after 15 minutes.

The final amount is highly dependent on the starting amount of delta ferrite since σ preferentially forms in the δ -ferrite regions. These results highlight the importance of controlling the processing temperatures during WAAM to minimize the permanence times at high temperatures, hence preventing delta-ferrite amount and the precipitation of undesirable phases, such as σ .

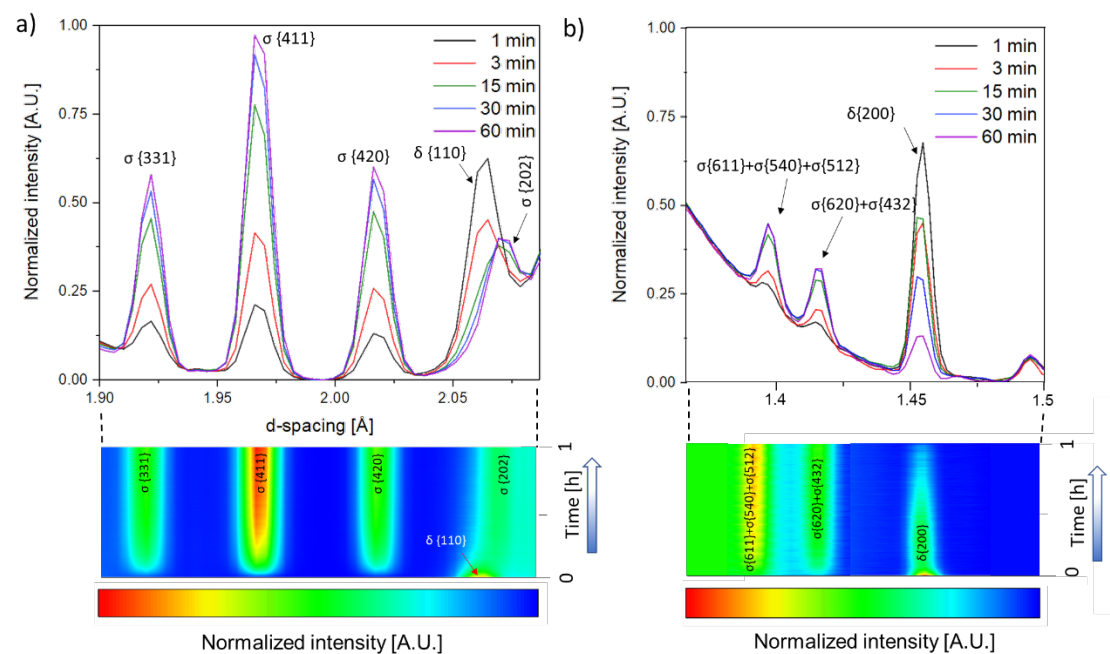


Figure 6 a) and b)- Sigma growth and delta ferrite dissolution in the isothermal stage at 950 °C after 1 min, 3 min, 15 min, 30 min, and 60 min.

The dilatometry results of the first hour of the heat treatment performed at 950 °C are depicted in Figure 7, and the intensity of the peaks was previously shown in Figure 6 a). The observed behavior illustrates that a slight contraction in the sample can be noticed during the first hour of isothermal holding. Rivolta et al. [32] showed that sigma precipitation from delta ferrite leads to a slight contraction in the dilatometric curve. This observation with the increase in sigma diffraction peaks, and the continuous dissolution of the $\{211\}_\delta$ peak results indicate a constant transformation of δ to σ during the isothermal stage of the heat treatment at 950 °C. The fast kinetics of δ to σ indicates that σ -growth is likely to be controlled by a small-scale atomic rearrangement of BCC into the tetragonal crystal structure, instead of long-range diffusion of substitutional alloying elements [33].

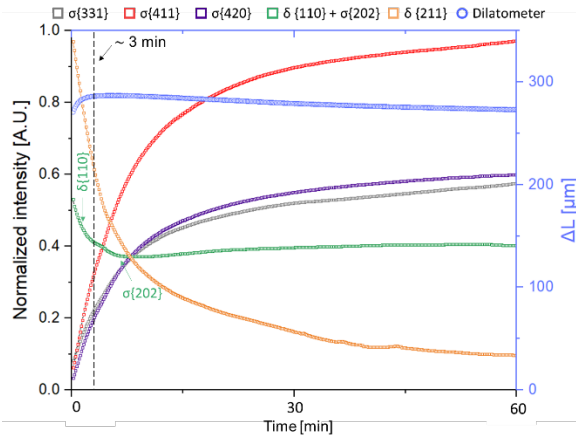


Figure 7 - Intensity evolution of the peaks $\{110\}_\delta$, $\{211\}_\delta$, $\{331\}_\sigma$, $\{411\}_\sigma$, $\{420\}_\sigma$ and $\{202\}_\sigma$ during the first hour of the isothermal holding at 950 °C.

After the two hours of heat treatment, no δ -ferrite peaks were found, as detailed in Figure 8. Analyzing Figure 6 to Figure 8, corresponding to the in-situ evolution of the 316 stainless WAAM part during heat treatment at 950 °C for 2 hours, clarifies the rapid mechanism of nucleation and growth of the σ phase at the expense of δ .

84 and 89 % (refer to the starting point in Figure 10 a). These differences in the ferrite content can be explained by the recursive alternation between vermicular and lathy ferrite in the samples before heat treatment, which may vary the content of ferrite. So, if the beam is analyzing a slightly different region on the material, minor changes in the delta ferrite amount can occur.

The volume percent of undissolved δ -ferrite was higher in the PWHT performed at 1050 °C than in the PWHT at 1200 °C. The undissolved amount of ferrite was approximately 6.5 % and 0.4 %, respectively. The continuous increase in the volume percent of austenite during isothermal holding at 1050 °C suggests that two hours were not enough to reach an equilibrium state, since thermodynamic equilibrium calculations (refer to Table 4) predict a complete dissolution of the ferrite phase at 1050 °C, and a residual amount of 2.6 % at 1200 °C. Two potential concurrent effects can explain this: i) the heat treatment time was not enough to reach an equilibrium condition; ii) the segregation of alloying elements during WAAM can locally change the material's chemistry, delaying the dissolution kinetics [34]. After solubilization at 1200 °C, only the stable {211} δ peak is observed, indicating a texture modification.

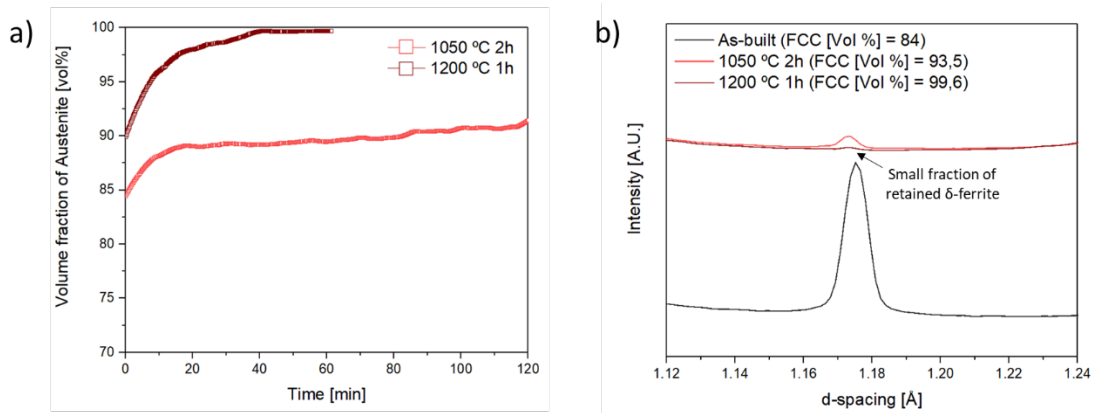


Figure 10 - a) Austenite volume percent during 1050 °C 2h and 1200 °C 1h; b) {200} δ reflection before and after solubilization heat treatment.

The final fraction of δ after the heat treatment decreases with an increase in the solubilization temperature. The complete dissolution of δ -ferrite in austenitic stainless steels can be hard to achieve since long heat treatment schedules are required [11,35].

Figure 11 a) details a colormap matrix containing the intensities of each peak during the heat treatments performed at 1200 °C, with the time along the y-axis and d-spacing along the x-axis. Due to the thermal expansion, the peaks shift to higher d-spacing values during heating.

Immediately after reaching the target heat treatment temperature, the intensity of the ferrite peaks decreased, becoming untraceable after 20 minutes of holding (refer to yellow arrows in Figure 11 a).

The lattice parameters calculated from the lattice spacing (d-spacing) for different $\{hkl\}$ planes are given for the higher intensity peaks of austenite in Figure 11 b). During isothermal holding, the lattice parameter expands, which is attributed to the dissolution of ferrite that changes the austenite composition [36,37].

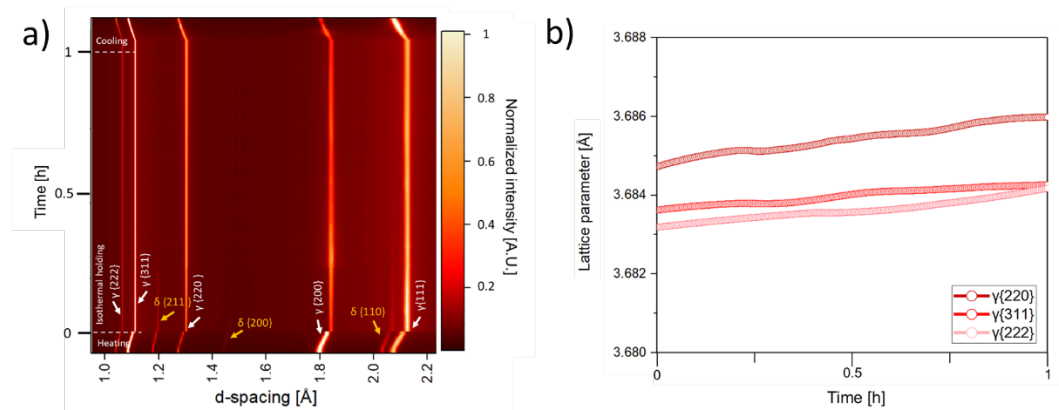


Figure 11 – a) Heatmap of isothermal holding at 1200 °C; b) Lattice parameter evolution of the prominent FCC peaks.

Thermodynamic equilibrium calculations based on the TCFE11 database of Thermo-Calc were used to predict the equilibrium phases of the steel using the nominal composition in tablex? Ou voces simplificaram elementos??. Figure 12 depicts the equilibrium phase diagram with isopleths for each equilibrium phase as a function of temperature and the Cr mass percentage. Red crosses mark the ER 316LSi composition for each heat-treatment temperature. It should be noticed that some discrepancies between the X-ray diffraction results and the equilibrium CalPhaD-based calculations exist. At 400 °C it is expected a 5% volume fraction of Laves, which was not found either by high-energy X-ray diffraction or microscopic analysis. Additionally, σ is not expected above 900 °C, thus the observed σ -phase at 950 °C during and after the heat treatment is in a metastable equilibrium state. Since δ – ferrite is thermodynamically metastable at temperatures where the σ precipitates, σ will preferentially grow from within the δ – ferrite causing its decomposition [33]. When the temperature rises to 1050 and 1200 °C the system evolves into an equilibrium state by solubilizing the δ – ferrite. The experimentally observed residual delta ferrite at 1050 and 1200 °C is not related to an equilibrium phase (formed above 1200 °C), but instead to insufficient decomposition. This can be explained since the selected heat treatment conditions are not equilibrium conditions: i. e.

the chosen time for the post-WAAM heat treatment is not enough to reach an equilibrium conditions.

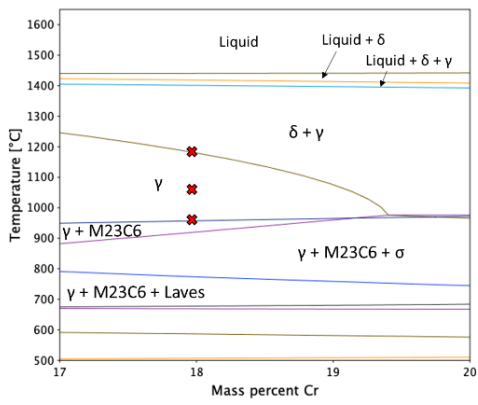
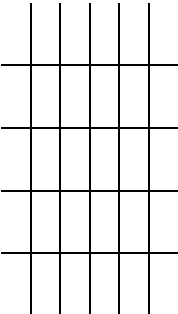


Figure 12 - Calculated isopleth for Cr mass percentage. The red crosses mark the composition of ER 316LSi at each heat-treatment temperature. The thermodynamic information is taken from the commercial thermodynamic database TCFE11.

3.4 Hardness measurements

Vickers hardness plots as a function of distance from the substrate are presented in Figure 13. As it can be seen, the higher hardness corresponds to the as-built and stress relieved sample (400 °C 1h), ranging from 170 to 200 HV. Higher temperatures resulted in a more significant dissolution of δ -ferrite, and therefore in lower hardness values. A maximum of 174 HV is observed for the heat-treated sample at 1050 °C, while a maximum of 163 HV was found in samples heat-treated at 1200 °C. Even though there is none δ -ferrite on the sample heat-treated at 950 °C, the slight difference between the means of this sample with the as-built condition is explained by the similar hardness of the σ -phase in comparison to that of δ -ferrite.

The stress-relieved sample had similar hardness values with the non-stress-relieved one and can be explained by the multiple thermal cycles developed during sample build-up. After one

layer is built, it is subjected to considerable periods at temperatures between 300-500 °C, thus experiencing an in-situ (at least partial) stress-relieving mechanism during production. The more predominant variable to affect the hardness is, therefore, the amount of δ ferrite, as the hardness values obtained for the two different solubilization temperatures are lower than for the other heat treatment conditions

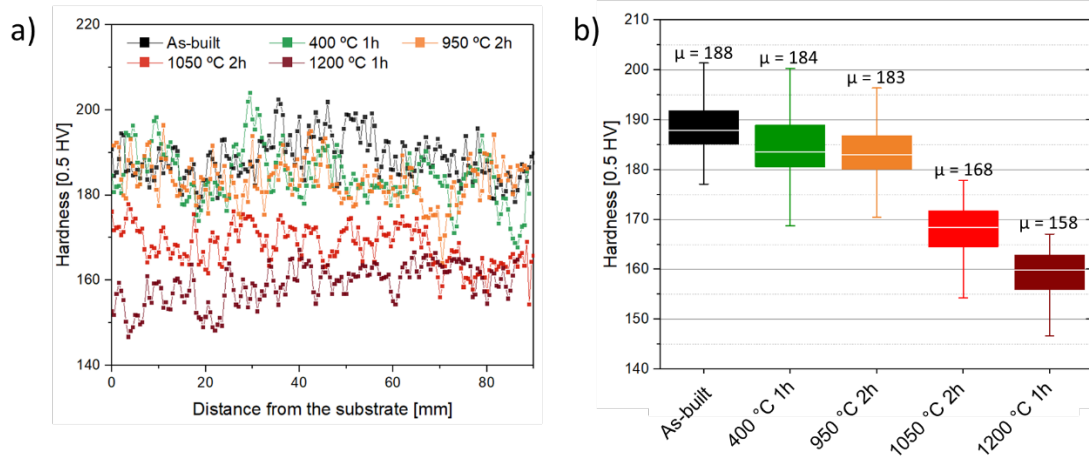


Figure 13 – a) Hardness measurements across sample's height, b) Boxplot of the hardness measurements displaying the minimum, maximum, median, and quartiles (Q1 and Q3) of each condition.

3.5 Electrical conductivity and magnetic permeability measurements

Eddy current testing (ECT) and four-point probe technique were used to evaluate magnetic permeability and electrical conductivity changes, respectively. Results are depicted in Figure 14. An inverse relation between the amount of δ -ferrite and the magnetic permeability was verified with ECT. With the gradual decrease of δ after PWHT at 1050 and 1200 °C, the signal output decreased. If there were not any X-ray diffraction measurements, δ -ferrite and σ phase could be qualitatively identified using ECT, as the magnetic permeability of the samples containing δ (as-built and heat-treated at 400 °C for 1h) are 3 orders of magnitude higher than the sample that includes the σ -phase (heat-treated at 950 °C 2h). Likewise, hardness measurements presented a similar trend.

The average measurements of the electrical conductivity of these samples are between 2.169 and 2.209 %IACS. The high standard deviation does not allow to establish any relationship between the amount of ferrite in a sample and the phases in it or with the grain size.

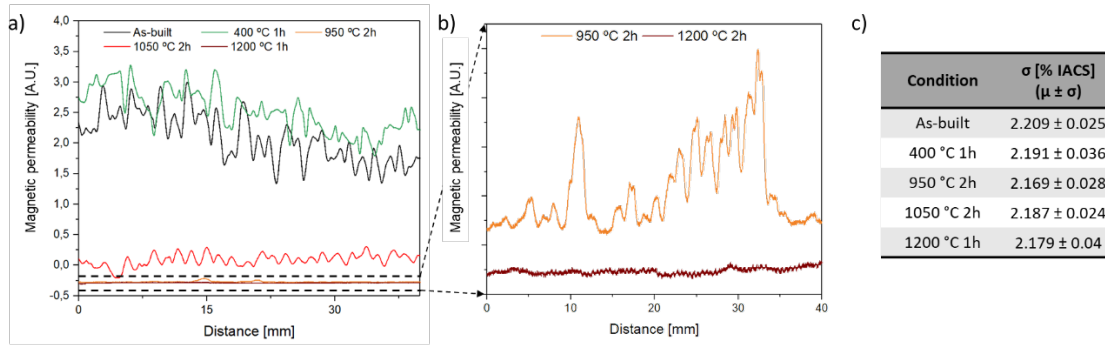


Figure 14 - a) Output signal of Eddy Current Testing (ECT) probe at 1.1 MHz, b) Detailed view of the signal output of ECT delineated with dashed lines, c) Average electrical conductivity measurements with a four-point probe for each condition.

Conclusions

A comprehensive study on the effect of post-WAAM heat treatments applied on 316L stainless steel was performed. By combining advanced microstructure characterization and in-situ measurements the following are the major findings of this work:

- The as-built WAAM samples presented an austenitic matrix with skeletal-type ferrite and lathy-ferrite aligned with the solidification direction (z-axis). No other secondary phases were discernible.
- After the stress relief at XX°C during xx h, the microstructure retained similar characteristics to that of the as-built condition. Synchrotron X-ray diffraction showed that both the δ - ferrite and austenite peaks shifted to lower scattering angles, evidencing a change in micro stain. This heat treatment decreased the sample hardness by an average of 4 HV.
- There is no clear morphological difference between the as-built sample and sample heat-treated at 950 °C for two hours. However, by synchrotron X-ray diffraction and electron backscatter diffraction, it was confirmed that delta ferrite acted as nucleation site for the precipitation of undesirable σ phase.
- In-situ observations showed that σ precipitation started within the first minutes of isothermal holding at 950 °C, and two hours was enough to fully transform $\delta \rightarrow \sigma$. A hardness decreased of 5 HV relative to the as-built sample was achieved.
- Thermodynamic calculations do not predict the existence of σ in the sample heat-treated at 950 °C. Insufficient kinetics for delta ferrite dissolution led to a metastable equilibrium condition, where sigma phase replaced the former vermicular delta ferrite structures.

- A temperature of 1050 °C showed to be enough to promote ferrite dissolution and compositional redistribution into the austenitic matrix, avoiding the precipitation of metastable σ . Efficient dissolution of δ -ferrite dendrites can be achieved with higher solubilization temperature, as heat treatments performed at 1050 and 1200 °C resulted in approximately 6.5 % and 0.4 % of δ -ferrite, respectively.
- Eddy's current testing was shown to be able to distinguish σ from δ - ferrite in the stainless steel WAAM parts. These results are promising for in situ inspection of large as-built components that cannot be easily segmented or transported.

Acknowledgments

TAR acknowledges FCT - MCTES for funding the Ph.D. grant SFRH/BD/144202/2019. VD acknowledges FCT - MCTES for funding the Ph.D. grant SFRH/BD/139454/2018. TAR, VD, RMM, TGS, and JPO acknowledge Fundação para a Ciência e a Tecnologia (FCT - MCTES) for its financial support via the project UID/00667/2020 (UNIDEMI). The São Paulo Research Foundation partially financed this study (FAPESP), grant No. 2019/00691-0.

References

- [1] S.J. Zinkle, G.S. Was, Materials challenges in nuclear energy, *Acta Mater.* 61 (2013) 735–758. <https://doi.org/10.1016/j.actamat.2012.11.004>.
- [2] R.K. Desu, H. Nitin Krishnamurthy, A. Balu, A.K. Gupta, S.K. Singh, Mechanical properties of Austenitic Stainless Steel 304L and 316L at elevated temperatures, *J. Mater. Res. Technol.* 5 (2016) 13–20. <https://doi.org/10.1016/j.jmrt.2015.04.001>.
- [3] H.P. Seifert, S. Ritter, H.J. Leber, Corrosion fatigue crack growth behaviour of austenitic stainless steels under light water reactor conditions, *Corros. Sci.* 55 (2012) 61–75. <https://doi.org/10.1016/j.corsci.2011.10.005>.
- [4] J.P. Oliveira, T.G. Santos, R.M. Miranda, Revisiting fundamental welding concepts to improve additive manufacturing: From theory to practice, *Prog. Mater. Sci.* 107 (2020) 100590. <https://doi.org/10.1016/j.pmatsci.2019.100590>.
- [5] J.A. Brooks, F.J. Lambert, Effects of Phosphorus, Sulfur and Ferrite Content on Weld Cracking of Type 309 Stainless Steel., *Weld. J. (Miami, Fla.)* 57 (1978).

- 486 [6] A. Ben Rhouma, T. Amadou, H. Sidhom, C. Braham, Correlation between microstructure
487 and intergranular corrosion behavior of low delta-ferrite content AISI 316L aged in the
488 range 550–700 °C, *J. Alloys Compd.* 708 (2017) 871–886.
489 <https://doi.org/10.1016/j.jallcom.2017.02.273>.
- 490 [7] J.C. Lippold, W.F. Savage, Solidification of Austenitic Stainless Steel Weldments - 3. the
491 Effect of Solidification Behavior on Hot Cracking Susceptibility., *Weld. J. (Miami, Fla.)*. 61
492 (1982) 388–396.
- 493 [8] P.D. Jablonski, J.A. Hawk, Homogenizing Advanced Alloys: Thermodynamic and Kinetic
494 Simulations Followed by Experimental Results, *J. Mater. Eng. Perform.* 26 (2017) 4–13.
495 <https://doi.org/10.1007/s11665-016-2451-3>.
- 496 [9] T.A. Rodrigues, V. Duarte, J.A. Avila, T.G. Santos, R.. Miranda, J.P. Oliveira, Wire and arc
497 additive manufacturing of HSLA steel: Effect of thermal cycles on microstructure and
498 mechanical properties, *Addit. Manuf.* 27 (2019) 440–450.
499 <https://doi.org/10.1016/j.addma.2019.03.029>.
- 500 [10] J.W. Elmer, T.A. Palmer, E.D. Specht, In situ observations of sigma phase dissolution in
501 2205 duplex stainless steel using synchrotron X-ray diffraction, *Mater. Sci. Eng. A.* 459
502 (2007) 151–155. <https://doi.org/10.1016/j.msea.2007.01.071>.
- 503 [11] A. Perron, C. Toffolon-Masclet, X. Ledoux, F. Buy, T. Guilbert, S. Urvoy, S. Bosonnet, B.
504 Marini, F. Cortial, G. Texier, C. Harder, V. Vignal, P. Petit, J. Farré, E. Suzon,
505 Understanding sigma-phase precipitation in a stabilized austenitic stainless steel
506 (316Nb) through complementary CALPHAD-based and experimental investigations,
507 *Acta Mater.* 79 (2014) 16–29. <https://doi.org/10.1016/j.actamat.2014.06.066>.
- 508 [12] M.J. Cieslak, A.M. Ritter, W.F. Savage, Chi-Phase Formation During Solidification and
509 Cooling of Cf-8M Weld Metal., *Weld. J. (Miami, Fla.)*. 63 (1984).
- 510 [13] A.D. Warren, I.J. Griffiths, P.E.J. Flewitt, Precipitation within localised chromium-
511 enriched regions in a Type 316H austenitic stainless steel, *J. Mater. Sci.* 53 (2018) 6183–
512 6197. <https://doi.org/10.1007/s10853-017-1748-4>.
- 513 [14] D.M. Escriba, E. Materna-Morris, R.L. Plaut, A.F. Padilha, Chi-phase precipitation in a
514 duplex stainless steel, *Mater. Charact.* 60 (2009) 1214–1219.
515 <https://doi.org/10.1016/j.matchar.2009.04.013>.

516 [15] T.F. de Andrade, A.M. Kliauga, R.L. Plaut, A.F. Padilha, Precipitation of Laves phase in a
517 28%Cr-4%Ni-2%Mo-Nb superferritic stainless steel, *Mater. Charact.* 59 (2008) 503–507.
518 <https://doi.org/10.1016/j.matchar.2007.03.006>.

519 [16] D.M.E. Villanueva, F.C.P. Junior, R.L. Plaut, A.F. Padilha, Comparative study on sigma
520 phase precipitation of three types of stainless steels: Austenitic, superferritic and
521 duplex, *Mater. Sci. Technol.* 22 (2006) 1098–1104.
522 <https://doi.org/10.1179/174328406X109230>.

523 [17] C.-C. Hsieh, W. Wu, Overview of Intermetallic Sigma (σ) Phase Precipitation in Stainless
524 Steels, *ISRN Metall.* 2012 (2012) 1–16. <https://doi.org/10.5402/2012/732471>.

525 [18] K.W. Chan, S.C. Tjong, Effect of secondary phase precipitation on the corrosion
526 behavior of duplex stainless steels, *Materials (Basel)*. 7 (2014) 5268–5304.
527 <https://doi.org/10.3390/ma7075268>.

528 [19] A.N.F. & D.H. A. P. Hammersley, S. O. Svensson, M. Hanfland, Two-dimensional detector
529 software: From real detector to idealised image or two-theta scan, *High Press. Res.*
530 14:4–6 (1996) 235–248. <https://doi.org/10.1080/08957959608201408>.

531 [20] P. Crowther, C. Daniel, xrdfit: A Python package for fitting synchrotron X-ray diffraction
532 spectra, *J. Open Source Softw.* 5 (2020) 2381. <https://doi.org/10.21105/joss.02381>.

533 [21] J.D.J.D. Escobar, G.A.G.A. Faria, L. Wu, J.P. Oliveira, P.R. Mei, A.J.A.J. Ramirez, Austenite
534 reversion kinetics and stability during tempering of a Ti-stabilized supermartensitic
535 stainless steel: correlative in situ synchrotron x-ray diffraction and dilatometry, *Acta*
536 *Mater.* 138 (2017) 92–99. <https://doi.org/10.1016/j.actamat.2017.07.036>.

537 [22] E.G. Astafurova, M.Y. Panchenko, V.A. Moskvina, G.G. Maier, S. V. Astafurov, E. V.
538 Melnikov, A.S. Fortuna, K.A. Reunova, V.E. Rubtsov, E.A. Kolubaev, Microstructure and
539 grain growth inhomogeneity in austenitic steel produced by wire-feed electron beam
540 melting: the effect of post-building solid-solution treatment, *J. Mater. Sci.* 55 (2020)
541 9211–9224. <https://doi.org/10.1007/s10853-020-04424-w>.

542 [23] X. Chen, J. Li, X. Cheng, B. He, H. Wang, Z. Huang, Microstructure and mechanical
543 properties of the austenitic stainless steel 316L fabricated by gas metal arc additive
544 manufacturing, *Mater. Sci. Eng. A.* 703 (2017) 567–577.
545 <https://doi.org/10.1016/j.msea.2017.05.024>.

- 546 [24] J.W. Elmer, S.M. Allen, T.W. Eagar, Microstructural development during solidification of
547 stainless steel alloys, *Metall. Trans. A.* 20 (1989) 2117–2131.
548 <https://doi.org/10.1007/BF02650298>.
- 549 [25] N. Suutala, T. Takalo, Austenitic Stainless Steel Welds, *Metall. Trans. A. I* (1980) 717–
550 725.
- 551 [26] J.W. Fu, Y.S. Yang, J.J. Guo, Formation of a blocky ferrite in Fe-Cr-Ni alloy during
552 directional solidification, *J. Cryst. Growth.* 311 (2009) 3661–3666.
553 <https://doi.org/10.1016/j.jcrysgro.2009.05.007>.
- 554 [27] A. F. PADILHA, P. R. RIOS, Decomposition of Austenite in Austenitic Stainless Steels, *ISIJ*
555 *Int.* 42 (2002) 325–337.
- 556 [28] A.F. Padilha, D.M. Escriba, E. Materna-Morris, M. Rieth, M. Klimenkov, Precipitation in
557 AISI 316L(N) during creep tests at 550 and 600 °C up to 10 years, *J. Nucl. Mater.* 362
558 (2007) 132–138. <https://doi.org/10.1016/j.jnucmat.2006.12.027>.
- 559 [29] J.R.Y. T.H. Chen, Effects of solution treatment and continuous cooling on γ -phase
560 precipitation in a 2205 duplex stainless steel, *J. Nucl. Mater.* 311 (2006) 220.
- 561 [30] J.W. Elmer, T.A. Palmer, E.D. Specht, Direct observations of sigma phase formation in
562 duplex stainless steels using In-situ synchrotron X-ray diffraction, *Metall. Mater. Trans.*
563 *A Phys. Metall. Mater. Sci.* 38 (2007) 464–475. [https://doi.org/10.1007/s11661-006-](https://doi.org/10.1007/s11661-006-9076-3)
564 [9076-3](https://doi.org/10.1007/s11661-006-9076-3).
- 565 [31] J.P. Oliveira, F.M.B. Fernandes, R.M. Miranda, N. Schell, J.L. Ocaña, Residual stress
566 analysis in laser welded NiTi sheets using synchrotron X-ray diffraction, *Mater. Des.* 100
567 (2016) 180–187. <https://doi.org/10.1016/j.matdes.2016.03.137>.
- 568 [32] B. Rivolta, R. Gerosa, F. Tavasci, The dilatometric technique for studying sigma phase
569 precipitation kinetics in F55 steel grade, *J. Therm. Anal. Calorim.* 132 (2018) 869–877.
570 <https://doi.org/10.1007/s10973-017-6940-x>.
- 571 [33] S. Atamert, J.E. King, Sigma-phase formation and its prevention in duplex stainless
572 steels, *J. Mater. Sci. Lett.* 12 (1993) 1144–1147. <https://doi.org/10.1007/BF00420548>.
- 573 [34] A. Caballero, J. Ding, S. Ganguly, S. Williams, Wire + Arc Additive Manufacture of 17-4
574 PH stainless steel: Effect of different processing conditions on microstructure, hardness,

575 and tensile strength, J. Mater. Process. Technol. 268 (2019) 54–62.
576 <https://doi.org/10.1016/j.jmatprotec.2019.01.007>.

577 [35] T.P.S. Gill, M. Vijayalakshmi, J.B. Gnanamoorthy, K.A. Padmanabhan, Transformation of
578 Delta-Ferrite During the Postweld Heat Treatment of Type 316L Stainless Steel Weld
579 Metal., Weld. J. (Miami, Fla). 65 (1986) 122–128.

580 [36] A. Bénéteau, P. Weisbecker, G. Geandier, E. Aeby-Gautier, B. Appolaire, Austenitization
581 and precipitate dissolution in high nitrogen steels: An in situ high temperature X-ray
582 synchrotron diffraction analysis using the Rietveld method, Mater. Sci. Eng. A. 393
583 (2005) 63–70. <https://doi.org/10.1016/j.msea.2004.09.054>.

584 [37] D. Manova, S. Mändl, H. Neumann, B. Rauschenbach, Analysis of in situ XRD
585 measurements for low energy ion beam nitriding of austenitic stainless steel, Surf.
586 Coatings Technol. 256 (2014) 64–72. <https://doi.org/10.1016/j.surfcoat.2014.03.047>.

587